

Bayesian analysis of the hardening in AMS-02 nuclei spectra

Jia-Shu Niu,^{1,2,*} Tianjun Li,^{2,†} and Hui-Fang Xue³

¹*Institute of Theoretical Physics, Shanxi University, Taiyuan, 030006, China*

²*CAS Key Laboratory of Theoretical Physics, Institute of Theoretical Physics, Chinese Academy of Sciences, Beijing, 100190, China*

³*Department of Astronomy, Beijing Normal University, Beijing 100875, China*

(Dated: July 22, 2022)

Based on the precision nuclei data released by AMS-02, the spectra hardening of both the primary (proton, helium, carbon, and oxygen) and the secondary (anti-proton, lithium, beryllium, and boron) cosmic ray (CR) nuclei have been studied in this work. With the diffusion-reacceleration model, we use 2 schemes to reproduce the hardening in the spectra: (i) adding a high-rigidity break in primary source injection; (ii) adding a high-rigidity break in diffusion coefficient. The global fitting results show that both schemes could reproduce the spectra hardening in current status. More multi-TV data is needed if one wants to distinguish these two schemes. In our global fitting, each of the nuclei species is allocated an independent solar modulation potential and a re-scale factor (which accounts for the isotopic abundance for primary nuclei and uncertainties of production cross section for secondary nuclei). The fitted values of these two parameter classes show us some hints on some new directions in CR physics. Particularly, it shows that beryllium has the specificity not only on its propagation in heliosphere, but also on the production cross section. This might be related to some problems in stellar physics and cosmology and needs further researches.

I. INTRODUCTION

Understanding the spectral features in cosmic rays (CRs) is of fundamental importance for studying their origin and propagation. Great progress in cosmic ray (CR) spectrum measurement has been made in recent years with new a generation of space-borne and ground-based experiments in operation. The fine structure of spectral hardening for primary nuclei at ~ 300 GV was observed by ATIC-2 [1], CREAM [2], PAMELA [3], and AMS-02 [4, 5].

Recently, AMS-02 has released the energy spectra of He, C, and O [6], which confirm the spectral hardening of CR primary nuclei. Moreover, the subsequently released energy spectra of Li, Be, and B [7] show that the secondary nuclei spectra harden even more than that of the primary ones at a few hundred GV. Because the secondary CR particles are produced in collisions of primary CR particles with interstellar medium (ISM), combining these data together would provide us a excellent opportunity to study the hardening of the CR nuclei spectra quantitatively.

Some previous works have proposed different solutions to this problem: (i) adding a new break in high-energy region (~ 300 GV) to the injection spectra (see, e.g., [8–12]); (ii) adding a new in high-rigidity break to the diffusion coefficient (see, e.g., [13]); (iii) inhomogeneous diffusion (see, e.g., [14–19]); (iv) the superposition of local and distant sources (see, e.g., [20–23]).

In this work, we do a global fitting on these primary and secondary nuclei spectra from AMS-02. Two

schemes are considered: (i) the hardening of the observed spectra comes from the sources (the breaks are already present in the spectra after the CR particles accelerated at the sources) – a new high-rigidity break is added in the primary source injections (Scheme I); (ii) the hardening of the observed spectra comes from the propagation – a new high-rigidity break is added in the diffusion coefficient (Scheme II). We hope that the precise spectra data from AMS-02 would give us a clear result, at least a tendency.

The paper is organized as follows. We first list the setups in Sec. II. The fitting results are give in Sec. III. Then we present some discussions and conclusions in Sec. IV.

II. SETUPS

In this section, we list some of the most important setups in this work, more detailed similar configurations could be found in Niu and Li [24].

A. Model

As in our previous work [10, 24], we use independent primary source spectra settings for proton and other nuclei species because of the significant difference observed in the slopes of proton and other nuclei species when $Z > 1$ [4–6]. Moreover, in our calculation, a cylindrically symmetric geometry is assumed to describe CR propagation in the galaxy, with a fixed maximum radius $r = 20$ kpc.

* jsniu@sxu.edu.cn

† tli@itp.ac.cn

1. Propagation Model

The diffusion-reacceleration model is used in the global fitting, which is widely used and can give consistent fitting results to the AMS-02 nuclei data (see, e.g., [24–26]). v_A is used to characterize the reacceleration, and z_h represents the half-height of the propagation region in the galaxy for the cylindrical coordinate system. In the whole propagation region, a uniform diffusion coefficient is used which depends on CR particles' rigidity.

In Scheme I, the diffusion coefficient is parametrized as

$$D_{xx}(R) = D_0 \beta \left(\frac{R}{R_0} \right)^\delta, \quad (1)$$

where β is the velocity of the particle in unit of light speed c , R_0 is the reference rigidity (4 GV), and $R \equiv pc/Ze$ is the rigidity.

For Scheme II, the diffusion coefficient is parametrized as

$$D_{xx}(R) = D_0 \cdot \beta \left(\frac{R_{br}}{R_0} \right) \times \begin{cases} \left(\frac{R}{R_{br}} \right)^{\delta_1} & R \leq R_{br} \\ \left(\frac{R}{R_{br}} \right)^{\delta_2} & R > R_{br} \end{cases}, \quad (2)$$

where R_{br} is the high-rigidity break; δ_1 and δ_2 are the diffusion slopes below and above the break.

2. Primary Sources

The primary source injection spectra of all kinds of nuclei are assumed to be a broken power law form. In Scheme I, it is represented as:

$$q_i = N_i \times \begin{cases} \left(\frac{R}{R_{A1}} \right)^{-\nu_{A1}} & R \leq R_{A1} \\ \left(\frac{R}{R_{A1}} \right)^{-\nu_{A2}} & R_{A1} < R \leq R_{A2} \\ \left(\frac{R}{R_{A2}} \right)^{-\nu_{A3}} \left(\frac{R_{A2}}{R_{A1}} \right)^{-\nu_{A2}} & R > R_{A2} \end{cases}, \quad (3)$$

where i denotes the species of nuclei, N_i is the normalization constant proportional to the relative abundance of the corresponding nuclei, and $\nu_A = \nu_{A1}(\nu_{A2}, \nu_{A3})$ for the nucleus rigidity R in the region divided by 2 breaks at the reference rigidity R_{A1} and R_{A2} . In this work, we use independent proton injection spectrum, and the corresponding parameters are R_{p1} , R_{p2} , ν_{p1} , ν_{p2} , and ν_{p3} . All the $Z > 1$ nuclei are assumed to have the same value of injection parameters.

For Scheme II, we have

$$q_i = N_i \times \begin{cases} \left(\frac{R}{R_A} \right)^{-\nu_{A1}} & R \leq R_A \\ \left(\frac{R}{R_A} \right)^{-\nu_{A2}} & R > R_A \end{cases}, \quad (4)$$

which are described by one break at the rigidity R_A (R_p) and two slopes below (ν_{A1} or ν_{p1}) and above (ν_{A2} or ν_{p2}) it.

3. Solar modulation

We adopt the force-field approximation [27] to describe the effects of solar modulation in the solar system, which contains only one parameter the so-called solar-modulation potential ϕ . Considering the charge-sign and suspected nuclei species dependence of the solar modulation which is represented in previous fitting [24], we adopt ϕ_p , ϕ_{He} , ϕ_C , ϕ_O , $\phi_{\bar{p}}$, ϕ_{Li} , ϕ_{Be} , and ϕ_B to modulate the proton, He, C, O, \bar{p} , Li, Be, and B nuclei data, respectively. This would give us the limitation of force-field approximation as a simple and effective theory to describe the solar modulation on local interstellar spectra (LIS).

4. Numerical tools

The public code GALPROP v56¹ [28–32] is used to solve the diffusion equation numerically. In view of some discrepancies when fitting with the new data which use the default primary source (injection) isotopic abundances in GALPROP [33], we use factors c_{He} , c_C , and c_O to re-scale the helium-4, carbon-12, and oxygen-16 abundance. At the same time, $c_{\bar{p}}$, c_{Li} , c_{Be} , and c_B are employed to re-scale the uncertainties from the \bar{p} , Li, Be, and B's production cross sections. Here, we expect that a constant factor is a simple assumption, which would help us to get a better fitting result.

B. Data Sets and Parameters

In our work, the proton flux (from AMS-02 and CREAM [2, 4]), helium flux (from AMS-02 and CREAM [2, 5]), carbon flux (from AMS-02 [6]), oxygen flux (from AMS-02 [6]), anti-proton flux (from AMS-02 [34]), lithium flux (from AMS-02 [7]), beryllium flux (from AMS-02 [7]), and boron flux (from AMS-02 [7]) are added in the global fitting data set. The CREAM data is used as the supplement of the AMS-02 data because it is more compatible with the AMS-02 data when $R \gtrsim 1$ TV. The errors used in our global fitting are the quadratic sum of statistical and systematic errors.

Altogether, the data set in our global fitting is

$$D = \{ D_p^{\text{AMS-02}}, D_{He}^{\text{AMS-02}}, D_C^{\text{AMS-02}}, D_O^{\text{AMS-02}}, D_{\bar{p}}^{\text{AMS-02}}, D_{Li}^{\text{AMS-02}}, D_{Be}^{\text{AMS-02}}, D_B^{\text{AMS-02}}, D_p^{\text{CREAM}}, D_{He}^{\text{CREAM}} \}.$$

¹ <http://galprop.stanford.edu>

The parameter sets for Scheme I is

$$\begin{aligned} \theta_1 = & \{D_0, \delta, z_h, v_A, | \\ & R_{p1}, R_{p2}, \nu_{p1}, \nu_{p2}, \nu_{p3}, \\ & R_{A1}, R_{A2}, \nu_{A1}, \nu_{A2}, \nu_{A3}, | \\ & N_p, c_{He}, c_C, c_O, c_{\bar{p}}, c_{Li}, c_{Be}, c_B, | \\ & \phi_p, \phi_{He}, \phi_C, \phi_O, \phi_{\bar{p}}, \phi_{Li}, \phi_{Be}, \phi_B\} , \end{aligned}$$

for Scheme II is

$$\begin{aligned} \theta_2 = & \{D_0, R_{br}, \delta_1, \delta_2, z_h, v_A, | \\ & R_p, \nu_{p1}, \nu_{p2}, R_A, \nu_{A1}, \nu_{A2}, | \\ & N_p, c_{He}, c_C, c_O, c_{\bar{p}}, c_{Li}, c_{Be}, c_B, | \\ & \phi_p, \phi_{He}, \phi_C, \phi_O, \phi_{\bar{p}}, \phi_{Li}, \phi_{Be}, \phi_B\} . \end{aligned}$$

These parameters can be separated into four classes: the propagation parameters, the primary source injection parameters, the normalization parameters, and the solar modulation potentials. And their priors are chosen to be uniform distributions with the prior intervals given in Tables I and II.

III. FITTING RESULTS

As in our previous works [10, 24], we use the Markov Chain Monte Carlo (MCMC) to determine the posterior probability distribution of the parameters in Scheme I and II. We take the samples of the parameters as their posterior probability distribution function (PDF) after the Markov Chains have reached their equilibrium states. The best-fit results and the corresponding residuals of the primary nuclei flux for 2 schemes are showed in Fig. 1, and the corresponding results of the secondary nuclei flux are showed in Fig. 2.²

The best-fit values, statistical mean values, standard deviations and allowed intervals at 95% CL for the parameters in θ_1 and θ_2 are shown in Table I and Table II, respectively. For best-fit results of the global fitting, we got $\chi^2/d.o.f = 383.45/521$ for Scheme I and $\chi^2/d.o.f = 395.48/524$ for Scheme II.

Generally speaking, the largest deviations in the fitting results between Scheme I and II comes from the fitting results of proton flux (which have a $\Delta\chi^2 = \chi_{II,proton}^2 - \chi_{I,proton}^2 \simeq 12.6$) and helium flux (which have a $\Delta\chi^2 = \chi_{I,He}^2 - \chi_{II,He}^2 \simeq 9.4$). This might come from that in Scheme I, we use independent breaks and slopes to describe the hardening in proton and other nuclei species, which is obviously different. While in Scheme II, the differences are described by a single δ_2 , this lead

to $\chi_{I,proton}^2 < \chi_{II,proton}^2$. At the same time, because the slopes in He, C and O spectra have almost the same value, it is natural that the δ_2 would be largely influenced by these nuclei species in the global fitting, which leads to a result of $\chi_{I,He}^2 > \chi_{II,He}^2$.

In other cases, there are no obvious deviations between the results of the two schemes. Moreover, we can see that in Fig. 2, the predicted tendency of the secondary nuclei spectra is different between the two schemes. Scheme I predicts a softer spectra when $R \gtrsim 1$ TV than Scheme II. This would be tested by high-rigidity (> 1 TV) secondary nuclei data released in the future.

A. Propagation Parameters

The results of posterior probability distributions of the propagation parameters are show in Fig. 3 (Scheme I), and Fig. 4 (Scheme II).

The most obvious differences between the fitting results of the parameters in this work and some previous works (see, e.g., Niu and Li [24], Yuan *et al.* [25]) are the values of D_0 , z_h , δ , and v_A . Compared with our previous work [24], D_0 , z_h , and v_A have relatively larger values here (especially in Scheme I), while δ have a smaller value in this work. In view of the data sets and parameters configurations (the hardening of the spectra have been fully considered), the results in this work should have a higher level of confidence.

In Scheme I, the δ value obtained is obviously smaller than that in our previous work (in which $\delta \simeq 3.5 - 3.7$) [24]. This because the added breaks in the primary source injection of proton ($\sim 480 - 890$ GV) and other primary nuclei species ($\sim 400 - 620$ GV) could take charge of the observed hardening in their observed spectra, other than use only one break in the source injection and let the only δ compromise the different slopes in high energy regions in Niu and Li [24].

In Scheme II, we got a high-rigidity break at $\sim (450 - 700)$ GV in the diffusion coefficient, and a slope $\delta_2 \sim (0.13 - 0.17)$ above the break. Although the value of δ_1 is not in the same posterior distribution region as that in Génolini *et al.* [13] (which gave $\delta_1 \sim 0.5 - 0.7$), we got a similar value of $\Delta\delta = \delta_1 - \delta_2 \sim 0.14$. Considering the simplifications in Génolini *et al.* [13] to do calculation for catching the key points in their work, we could conclude that we get a consistent result compared with their work.

Moreover, whether a high-rigidity break in diffusion coefficient is needed in current AMS-02 nuclei data if we have already considered the high-rigidity break in primary source injection? Some conclusions are proposed in Yuan *et al.* [26]. It is δ value dependent. When $\delta \sim 0.3$, it is not needed such a break; while $\delta \sim 0.5 - 0.7$, such a break is needed to reproduce current spectra data.

Another point should be noted is that in Scheme II, the uncertainty of z_h could reach down to 0.05, which might be caused by the special configurations in this scheme (employing a break in diffusion coefficient to account for

² Considering the correlations between different parameters, we could not get a reasonable reduced χ^2 for each part of the data set independently. As a result, we show the χ^2 for each part of the data set in Figs. 1, 2.

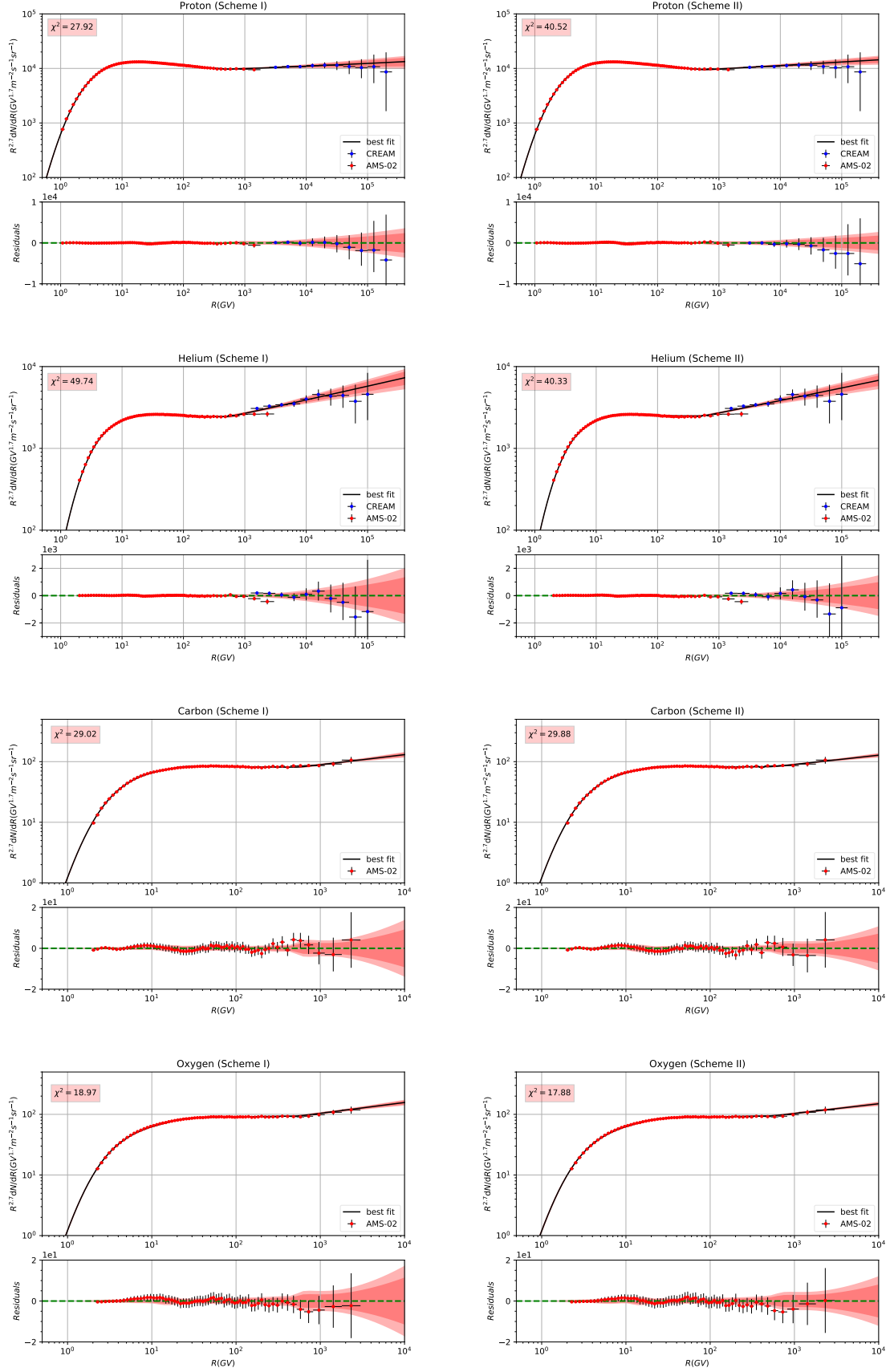


FIG. 1: The global fitting results and the corresponding residuals to the primary nuclei flux (proton flux, helium flux, carbon flux and oxygen flux) for 2 schemes. The 2σ (deep red) and 3σ (light red) bounds are also shown in the figures. The relevant χ^2 of each nuclei species is also shown in the sub-figures.

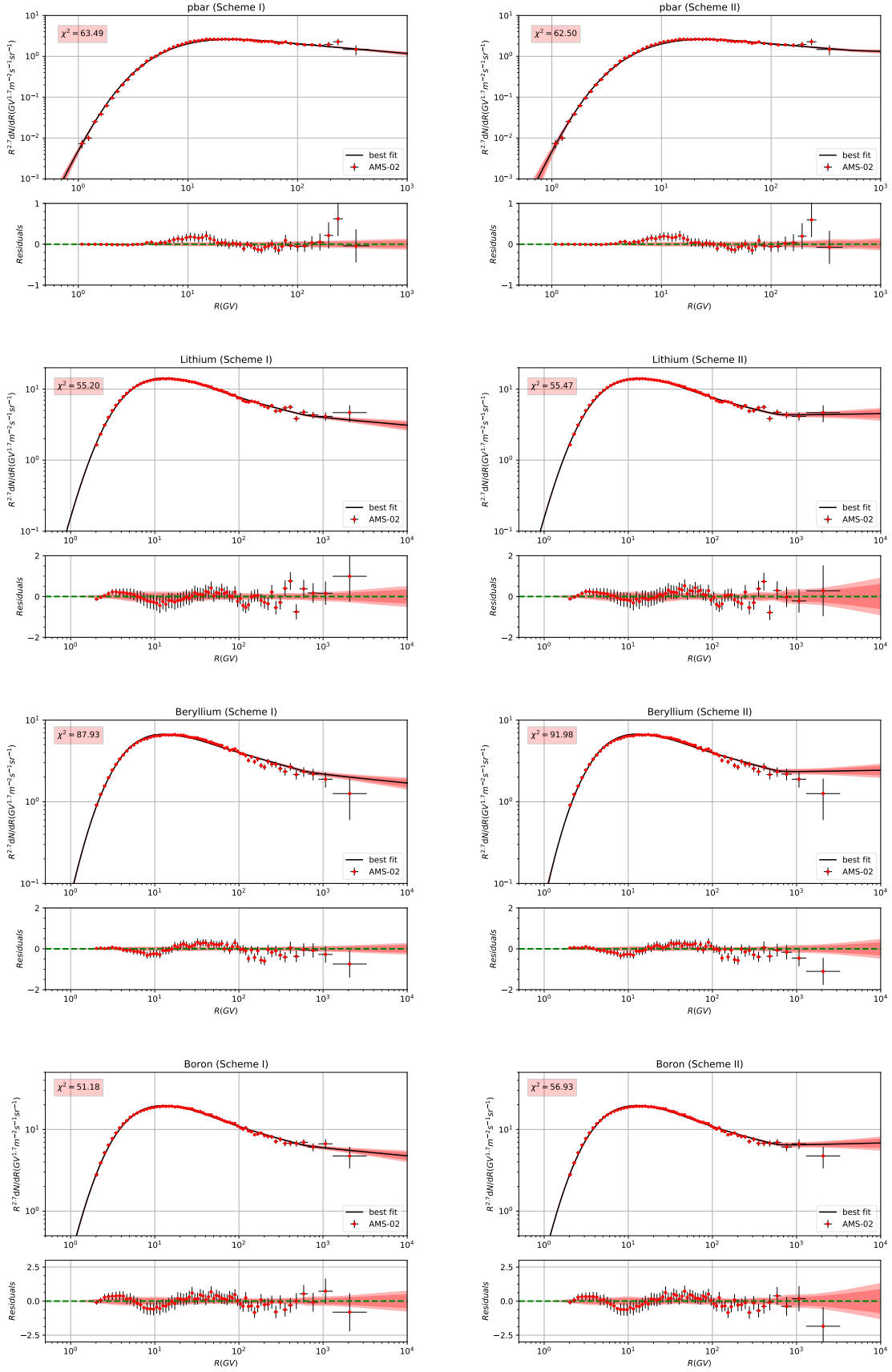


FIG. 2: The global fitting results and the corresponding residuals to the secondary nuclei flux (anti-proton flux, lithium flux, beryllium flux and boron flux) for 2 schemes. The 2σ (deep red) and 3σ (light red) bounds are also shown in the figures. The relevant χ^2 of each nuclei species is also shown in the sub-figures.

TABLE I: Constraints on the parameters in set θ_1 . The prior interval, best-fit value, statistic mean, standard deviation and the allowed range at 95% CL are listed for parameters. With $\chi^2/d.o.f = 383.45/521$ for best-fit result.

ID	Prior range	Best-fit value	Posterior mean and Standard deviation	Posterior 95% range
D_0 ($10^{28} \text{ cm}^2 \text{ s}^{-1}$)	[1, 30]	18.36	17.69 \pm 1.96	[14.58, 20.97]
δ	[0.1, 1.0]	0.284	0.284 \pm 0.005	[0.277, 0.293]
z_h (kpc)	[0.5, 30.0]	11.30	10.32 \pm 1.43	[7.85, 12.31]
v_A (km/s)	[0, 80]	56.89	57.74 \pm 2.76	[53.39, 62.31]
R_{p1} (GV)	[1, 30]	24.61	24.13 \pm 1.38	[21.48, 26.28]
R_{p2} (GV)	[60, 1000]	528.31	673.70 \pm 125.00	[484.97, 893.13]
ν_{p1}	[1.0, 4.0]	2.177	2.172 \pm 0.015	[2.145, 2.196]
ν_{p2}	[1.0, 4.0]	2.474	2.474 \pm 0.007	[2.463, 2.485]
ν_{p3}	[1.0, 4.0]	2.367	2.352 \pm 0.015	[2.326, 2.375]
R_{A1} (GV)	[1, 30]	22.23	21.47 \pm 1.06	[19.91, 23.43]
R_{A2} (GV)	[60, 1000]	540.03	504.07 \pm 68.20	[400.28, 622.79]
ν_{A1}	[1.0, 4.0]	2.096	2.082 \pm 0.015	[2.056, 2.107]
ν_{A2}	[1.0, 4.0]	2.411	2.409 \pm 0.006	[2.401, 2.420]
ν_{A3}	[1.0, 4.0]	2.252	2.259 \pm 0.015	[2.231, 2.283]
N_p^a	[1, 8]	4.45	4.45 \pm 0.02	[4.42, 4.48]
c_{He}	[0.1, 5.0]	0.643	0.645 \pm 0.004	[0.638, 0.652]
c_C	[0.1, 5.0]	0.551	0.553 \pm 0.005	[0.545, 0.561]
c_O	[0.1, 5.0]	0.504	0.504 \pm 0.008	[0.492, 0.518]
$c_{\bar{p}}$	[0.1, 5.0]	1.72	1.74 \pm 0.10	[1.58, 1.91]
c_{Li}	[0.1, 5.0]	1.43	1.44 \pm 0.07	[1.31, 1.57]
c_{Be}	[0.1, 5.0]	1.70	1.72 \pm 0.09	[1.57, 1.87]
c_B	[0.1, 5.0]	1.10	1.11 \pm 0.05	[1.03, 1.19]
ϕ_p (GV)	[0, 1.5]	0.70	0.70 \pm 0.02	[0.66, 0.74]
ϕ_{He} (GV)	[0, 1.5]	0.61	0.60 \pm 0.02	[0.56, 0.64]
ϕ_C (GV)	[0, 1.5]	0.72	0.71 \pm 0.02	[0.67, 0.75]
ϕ_O (GV)	[0, 1.5]	0.74	0.72 \pm 0.03	[0.68, 0.76]
$\phi_{\bar{p}}$ (GV)	[0, 1.5]	0.008	0.02 \pm 0.02	[0.001, 0.054]
ϕ_{Li} (GV)	[0, 1.5]	0.65	0.62 \pm 0.04	[0.56, 0.69]
ϕ_{Be} (GV)	[0, 1.5]	0.27	0.27 \pm 0.04	[0.20, 0.33]
ϕ_B (GV)	[0, 1.5]	0.63	0.62 \pm 0.04	[0.56, 0.69]

^a Post-propagated normalization flux of protons at 100 GeV in unit $10^{-2} \text{ m}^{-2} \text{ s}^{-1} \text{ sr}^{-1} \text{ GeV}^{-1}$

the hardening of all the primary and secondary spectra and not considering the differences between the spectra of proton and other species).

B. Primary Source Injection Parameters

The results of posterior probability distributions of the primary source injection parameters are show in Fig. 5 (Scheme I), and Fig. 6 (Scheme II).

Same as our previous works [10, 24], the rigidity breaks and slopes are obviously different between proton and other nuclei species in both schemes. Particularly, in Scheme I, the differences between the primary source injection high-rigidity slopes have values of $\nu_{p2} - \nu_{p3} \sim 0.1$ (for proton) and $\nu_{A2} - \nu_{A3} \sim 0.15$ (for other nuclei species). This indicate that if we want to ascribe the hardening of the spectra to the primary source injections, the acceleration mechanisms in this energy region (500 – 800 GV) should be different between proton and

other nuclei species.

In Scheme II, the hardening of the spectra is accounted by the break in diffusion coefficient, and the fitting results of the breaks and slopes in primary source injections are consistent with that in Scheme I. It shows us a good reliability of these fitted values.

C. Normalization Parameters

The results of posterior probability distributions of the normalization parameters are show in Fig. 7 (Scheme I), and Fig. 8 (Scheme II).

In Table I and II, we can find that the normalization parameters of the primary nuclei species have an uncertainty of $< 1\%$, and that of the secondary nuclei species $\sim 5\%$. This shows us the necessity to employ them in the global fitting. Although the fitted values of them have slight differences in Scheme I and II, the relative relations of them can be kept in both of the schemes.

TABLE II: Constraints on the parameters in set θ_2 . The prior interval, best-fit value, statistic mean, standard deviation and the allowed range at 95% CL are listed for parameters. With $\chi^2/d.o.f = 395.48/524$ for best-fit result.

ID	Prior range	Best-fit value	Posterior mean and Standard deviation	Posterior 95% range
D_0 ($10^{28} \text{ cm}^2 \text{ s}^{-1}$)	[1, 30]	18.27	17.98 \pm 1.22	[15.98, 19.94]
R_{br} (GV)	[200, 800]	541.73	559.80 \pm 73.35	[455.97, 693.90]
δ_1	[0.1, 1.0]	0.275	0.278 \pm 0.005	[0.269, 0.287]
δ_2	[0.1, 1.0]	0.139	0.148 \pm 0.013	[0.127, 0.170]
z_h (kpc)	[0.5, 30.0]	8.53	8.50 \pm 0.05	[8.42, 8.58]
v_A (km/s)	[0, 80]	65.66	65.04 \pm 3.80	[59.01, 71.27]
R_p (GV)	[1, 30]	27.88	26.56 \pm 1.83	[23.87, 29.38]
ν_{p1}	[1.0, 4.0]	2.203	2.191 \pm 0.016	[2.163, 2.217]
ν_{p2}	[1.0, 4.0]	2.494	2.487 \pm 0.007	[2.475, 2.498]
R_A (GV)	[1, 30]	20.71	20.84 \pm 0.79	[19.63, 22.20]
ν_{A1}	[1.0, 4.0]	2.073	2.066 \pm 0.014	[2.042, 2.087]
ν_{A2}	[1.0, 4.0]	2.407	2.406 \pm 0.006	[2.397, 2.416]
N_p^a	[1, 8]	4.49	4.47 \pm 0.02	[4.43, 4.51]
c_{He}	[0.1, 5.0]	0.644	0.646 \pm 0.004	[0.639, 0.653]
c_C	[0.1, 5.0]	0.551	0.552 \pm 0.005	[0.545, 0.560]
c_O	[0.1, 5.0]	0.497	0.500 \pm 0.007	[0.489, 0.512]
$c_{\bar{p}}$	[0.1, 5.0]	1.89	1.89 \pm 0.11	[1.70, 2.07]
c_{Li}	[0.1, 5.0]	1.53	1.52 \pm 0.08	[1.39, 1.65]
c_{Be}	[0.1, 5.0]	1.80	1.79 \pm 0.08	[1.65, 1.92]
c_B	[0.1, 5.0]	1.18	1.17 \pm 0.06	[1.08, 1.26]
ϕ_p (GV)	[0, 1.5]	0.73	0.72 \pm 0.03	[0.67, 0.76]
ϕ_{He} (GV)	[0, 1.5]	0.57	0.56 \pm 0.02	[0.52, 0.60]
ϕ_C (GV)	[0, 1.5]	0.69	0.67 \pm 0.03	[0.63, 0.72]
ϕ_O (GV)	[0, 1.5]	0.71	0.70 \pm 0.03	[0.65, 0.74]
$\phi_{\bar{p}}$ (GV)	[0, 1.5]	0.002	0.01 \pm 0.01	[0.0006, 0.0352]
ϕ_{Li} (GV)	[0, 1.5]	0.56	0.55 \pm 0.04	[0.48, 0.61]
ϕ_{Be} (GV)	[0, 1.5]	0.18	0.17 \pm 0.04	[0.10, 0.24]
ϕ_B (GV)	[0, 1.5]	0.56	0.56 \pm 0.04	[0.49, 0.62]

^a Post-propagated normalization flux of protons at 100 GeV in unit $10^{-2} \text{ m}^{-2} \text{ s}^{-1} \text{ sr}^{-1} \text{ GeV}^{-1}$

In order to get a clear comparison, we use a boxplot³ to represent all the c_i for Scheme I and II in Fig. 9. ⁴

Interestingly, the re-scale factors of all the primary nuclei species are > 1.0 , and all the secondary factors are < 1.0 . Remember that these c_i s represent the element abundances for the former and production cross section uncertainties for the latter. In Fig. 9, we can visually conclude that the most special c_i is c_B . In fact, c_B is the value which is most close to 1. In this regard, $c_{\bar{p}}$, c_{Li} , and c_{Be} should be given more attentions.

The value of $c_{\bar{p}}$ in this work ($\sim 1.7 - 1.9$) is obviously different from that in previous works ($\sim 1.3 - 1.4$), which could be explained by the usage of a single ϕ to modulate

all the nuclei species in them. Additionally, the value of $c_{\bar{p}}$ is also influenced even if we use a independent solar modulation potential $\phi_{\bar{p}}$ for \bar{p} , which have a negative charge and could not be handled by force-field approximation. In this view, $c_{\bar{p}}$ could not be considered as a pure value to describe the uncertainty of \bar{p} production cross section.

Besides $c_{\bar{p}}$, the following large deviation value is c_{Be} . Not like \bar{p} , the solar modulation could be well modeled in our fitting (see Fig. 10 and Fig. 11). We cannot find some other reasons to interpret its specificity tentatively, and this needs more attention in future study.

D. Solar Modulation Potentials

The results of posterior probability distributions of the solar modulation potentials are shown in Fig. 10 (Scheme I), and Fig. 11 (Scheme II). For convenience, the boxplot of all the ϕ_i s in Scheme I and II are shown in Fig. 12.

Like that in Fig. 9, the relative relations between these ϕ_i s in each schemes are kept stably. What is in-

³ A box plot or boxplot is a method for graphically depicting groups of numerical data through their quartiles. In our configurations, the band inside the box shows the median value of the dataset, the box shows the quartiles, and the whiskers extend to show the rest of the distribution which are edged by the 5th percentile and the 95th percentile.

⁴ Here, we remove the parameter N_p and show the results of the c_i s (which are called re-scale factors hereinafter).

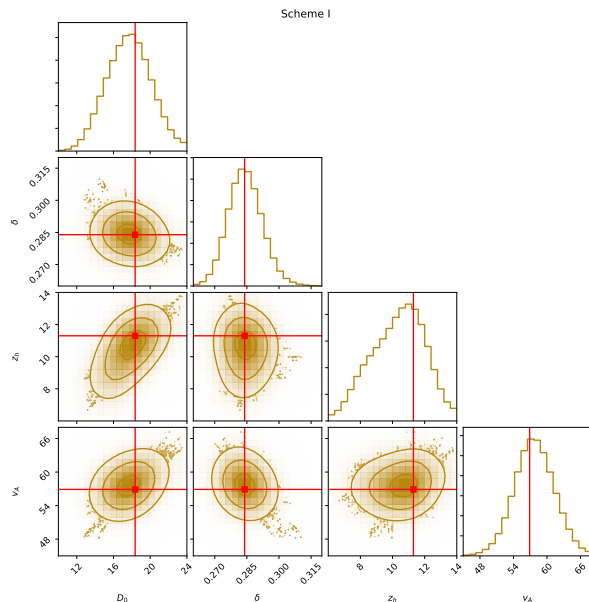


FIG. 3: Fitting 1D probability and 2D credible regions of posterior PDFs for the combinations of all propagation parameters from Scheme I. The regions enclosing σ , 2σ and 3σ CL are shown in step by step lighter golden. The red cross lines and marks in each plot indicates the best-fit value (largest likelihood).

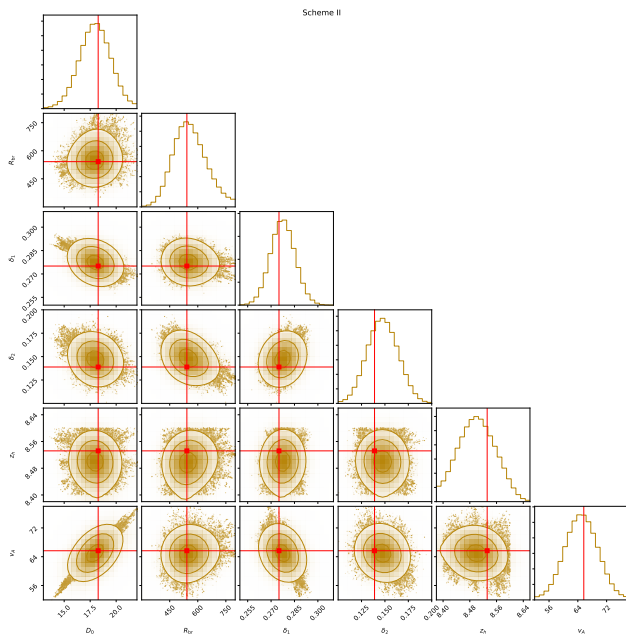


FIG. 4: Same as Fig. 3, but for Scheme II.

interesting is that, all these ϕ_i s have almost similar values ($0.5 - 0.7$ GV) except $\phi_{\bar{p}}$ and ϕ_{Be} . As we know, as an effective tool to handle solar modulation, force-field approximation is charge independent. The fitted values of $\phi_{\bar{p}}$ clearly show that this approximation cannot deal with

the solar modulation effects on \bar{p} at current data levels. Removing $\phi_{\bar{p}}$ not to talk, it is strange that ϕ_{Be} have a large deviation compared with other ϕ_i s. Considering the uncertainties and PDFs in Fig. 10 and Fig. 11, the values of ϕ_{Be} should be regarded seriously. The reasons and relevant physics behind ϕ_{Be} should be studied in further research.

IV. DISCUSSIONS AND CONCLUSIONS

In this work, we use the newly released data from AMS-02 [4–7, 34], to study the origin of the hardening in both the primary (proton, helium, carbon and oxygen) and secondary (anti-proton, lithium, beryllium and boron) CR nuclei spectra based on 2 different schemes. Global fitting results have shown that, both of the schemes could give an effective fitting on the current primary and secondary nuclei spectra from AMS-02, and could reproduce the hardening of the spectra obviously. More precise secondary nuclei data on high energy regions ($\gtrsim 1$ TV) is needed to distinguish these two schemes.

In our global fitting, each kind of the species has employed an independent solar modulation potential ϕ_i to account for the effects of solar modulation, which is based on the force-field approximation. As a widely used and effective treatment on solar modulation, such configuration could show us its limitations. In most of the situations, it could give us an acceptant result.⁵ If we want to study the fine structures in low-energy regions of the spectra ($\lesssim 30$ GV), we should consider more effects in solving the Parker transport equation which contains diffusion, convection, particle drift and energy loss (see, e.g., Boschini et al. [36]). On the other hand, the different fitted values of ϕ_i for different nuclei species indicate some of the species really experience different physical processes in the heliosphere. Especially for beryllium, it needs further researches to reveal the physics behind the value of ϕ_{Be} .⁶

Another interesting aspect comes from the fitted values of the re-scale factors. All the primary nuclei abundances have the values of the re-scale factors (which represent their relative element abundances) of $\sim (0.5 - 0.6)$. We know that in GALPROP, the primary source (injection) isotopic abundances are taken first as the solar system abundances, which are iterated to achieve an agreement with the propagated abundances as provided by ACE at ~ 200 MeV/nucleon [37, 38] assuming a propagation model. As a result, it is natural that the abundance of the CR species in the solar system (relatively low-rigidity

⁵ Except the situation for anti-proton flux, it comes from the charge-sign dependence of the solar modulation, which cannot be handled by force-field approximation.

⁶ Here we exclude another special species – anti-proton, whose particularity would mainly be generated by its negative charge.

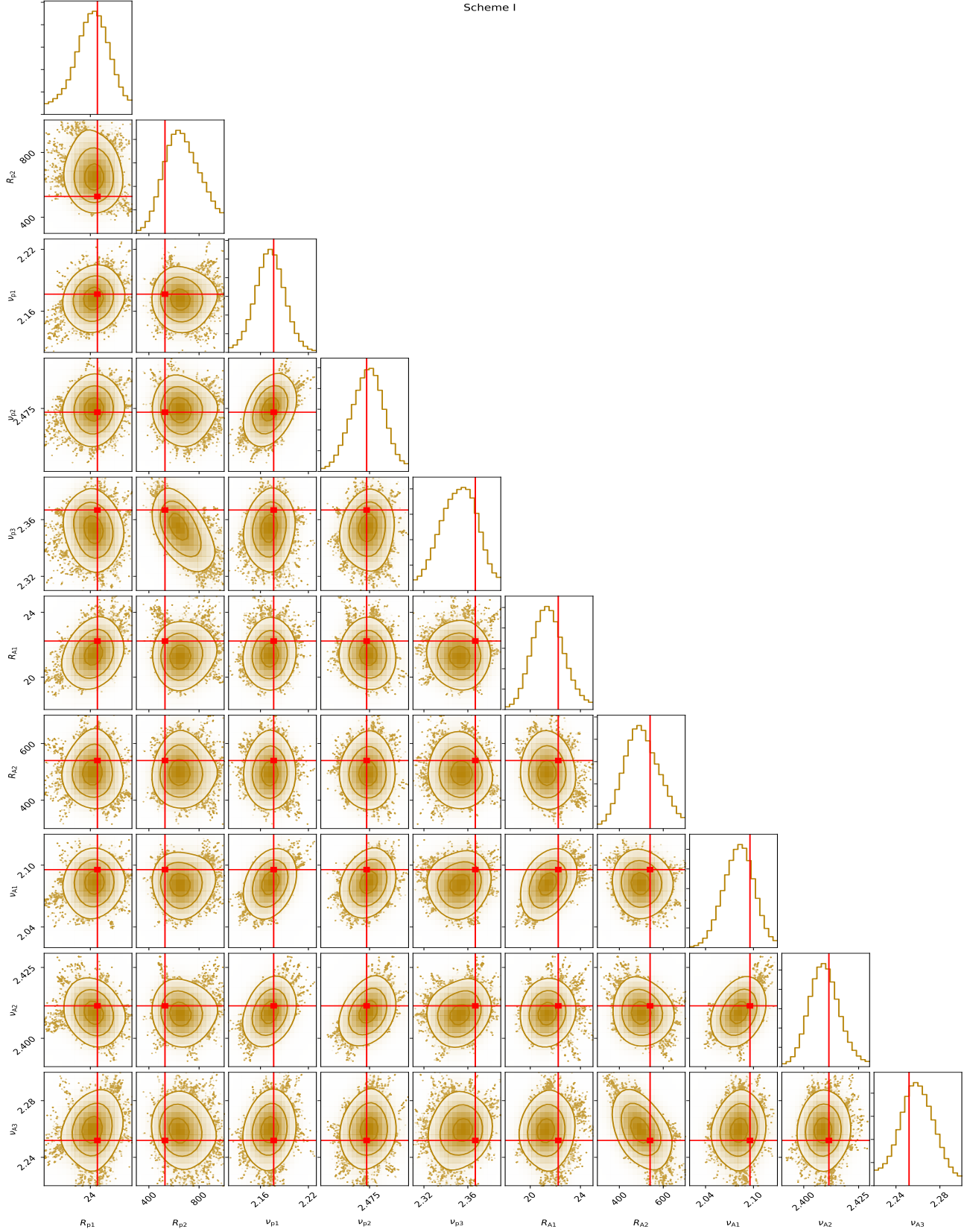


FIG. 5: Fitting 1D probability and 2D credible regions of posterior PDFs for the combinations of all primary source injection parameters from Scheme I. The regions enclosing σ , 2σ and 3σ CL are shown in step by step lighter golden. The red cross lines and marks in each plot indicates the best-fit value (largest likelihood).

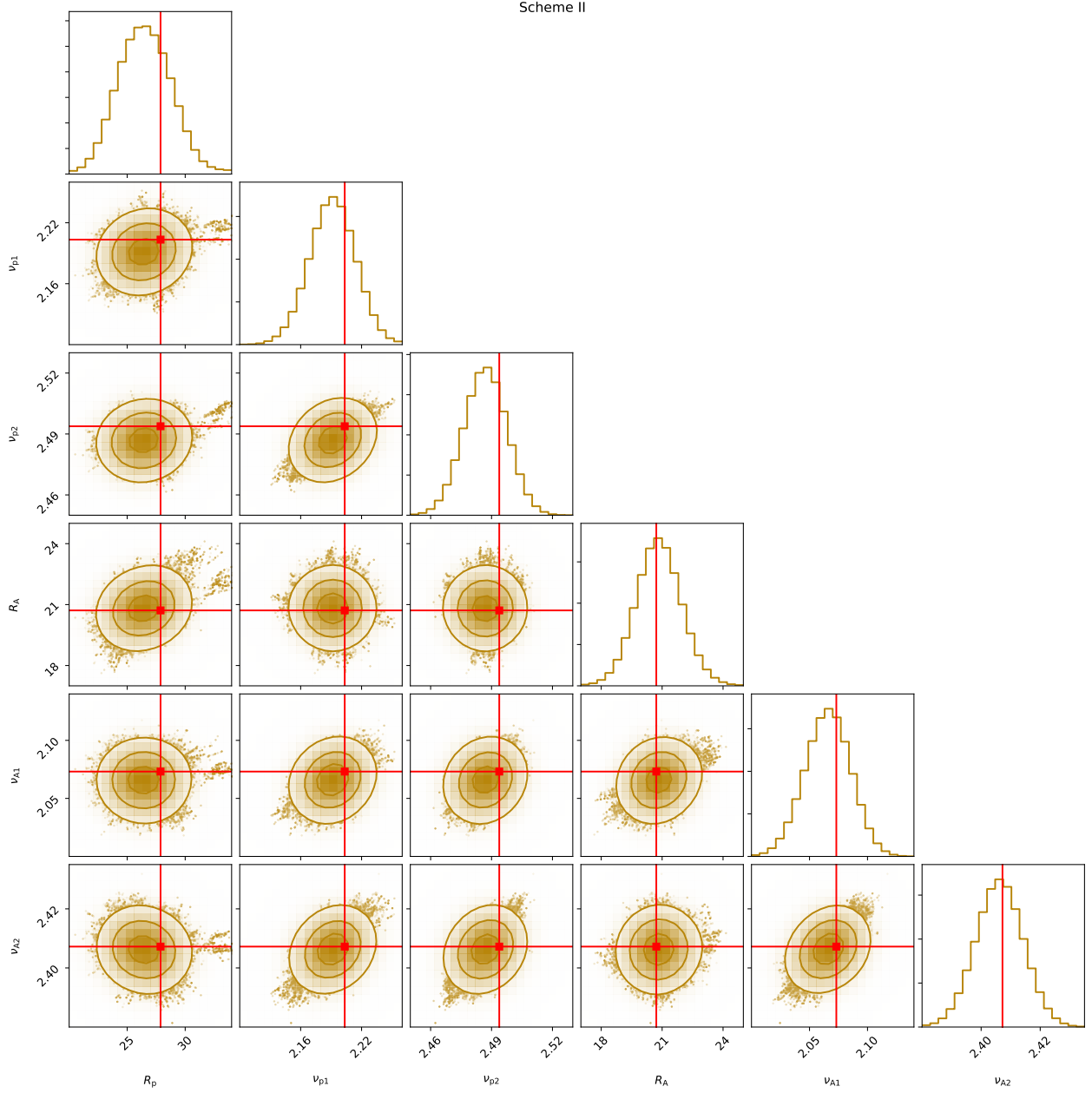


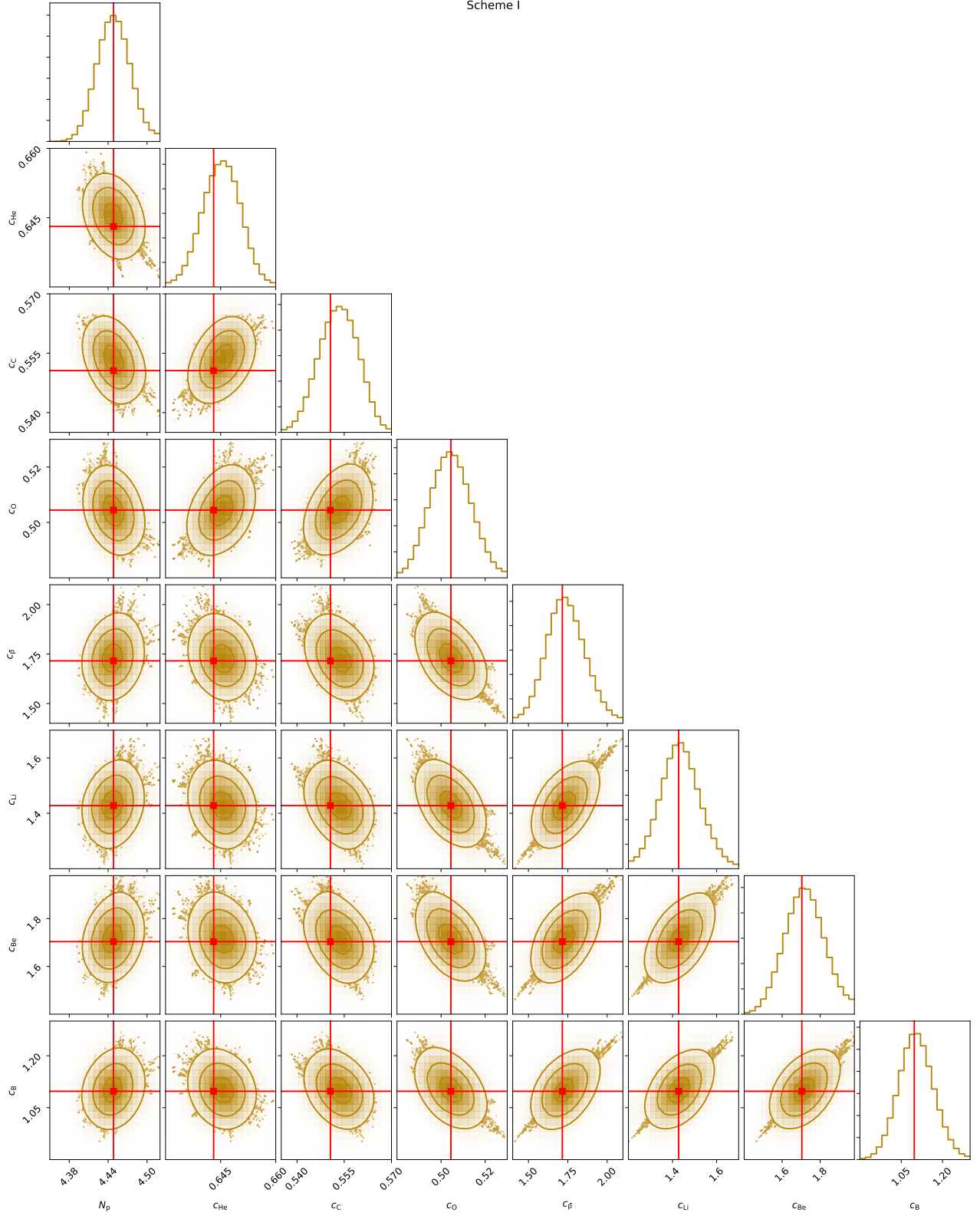
FIG. 6: Same as Fig. 5, but for Scheme II.

CR particles) is different from that in outer spaces (relatively high-rigidity CR particles). This provides us an effective and independent way to study the isotopic abundance out of the solar system. Moreover, all the re-scale factors of the secondary nuclei species (which represent the uncertainties of their production cross sections) are larger than 1.0, some of them can reach up to $1.7 \sim 1.8$ ($c_{\bar{p}}$ and c_{Be}). This would lead to further studies on these cross sections on colliders and would open a new door to

study nuclear physics.⁷

Note: Excluding the fitted values of $c_{\bar{p}}$ and $\phi_{\bar{p}}$ for anti-proton's negative charge, we find that the most special species is beryllium, not only its propagation in heliosphere, but also its production cross section. This would be related to some interesting problems in stellar physics and cosmology on such special element, which needs further research based on more precise CR data.

⁷ One such pioneering work can be found in Génolini *et al.* [39].



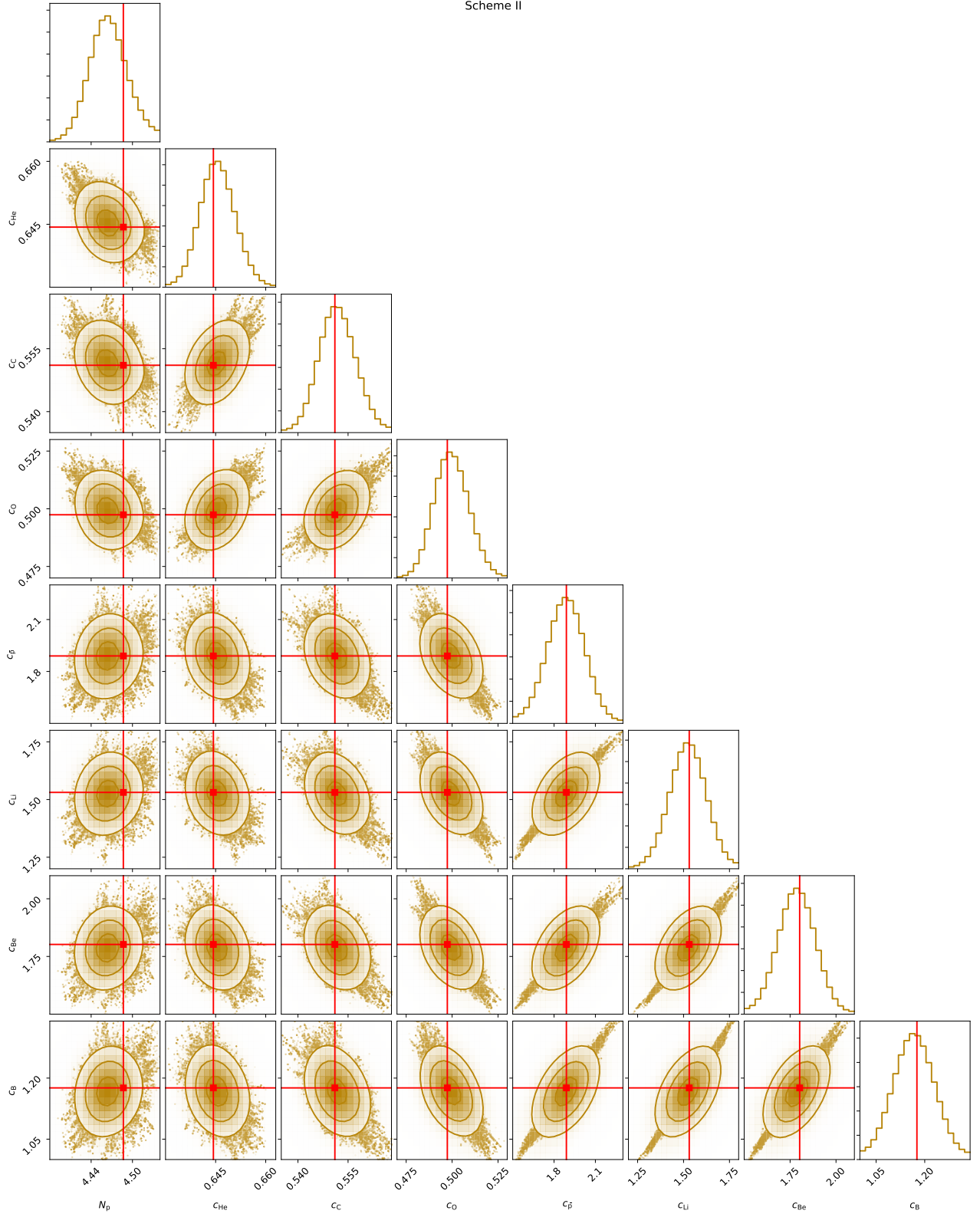


FIG. 8: Same as Fig. 7, but for Scheme II.

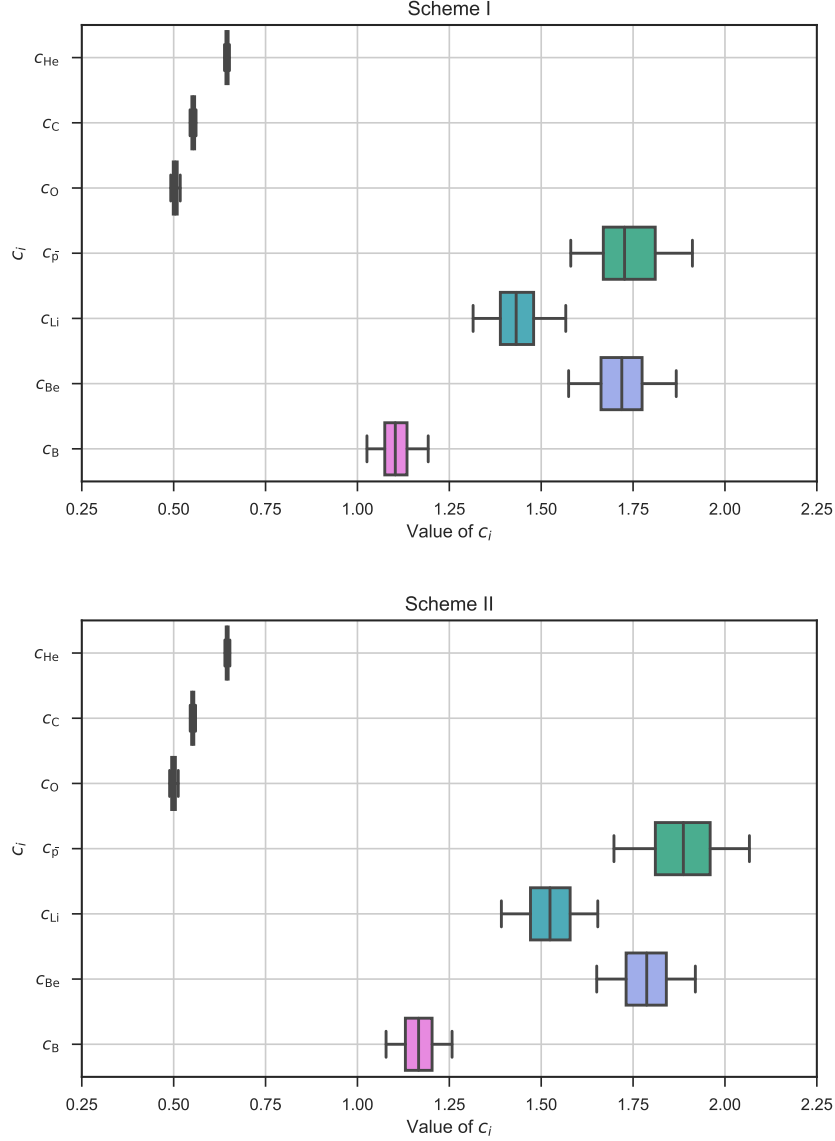


FIG. 9: The boxplot for the re-scale factors (c_i s) in Scheme I and II.

ACKNOWLEDGMENTS

We would like to thank Qiang Yuan very much for helpful discussions, Maurin et al. [40] to collect database and associated online tools for charged cosmic-ray measurements, and Foreman-Mackey et al. [41] to provide us the tool to visualize multidimensional samples using a

scatterplot matrix. JSN want to appreciate Yi-Hang Nie and Jiu-Qin Liang for their trusts and supports. This research was supported in part by the Projects 11475238 and 11647601 supported by National Science Foundation of China, and by Key Research Program of Frontier Sciences, CAS. The calculation in this paper are supported by HPC Cluster of SKLTP/ITP-CAS.

-
- [1] A. D. Panov, J. H. Adams, H. S. Ahn, G. L. Bashindzhagyan, K. E. Batkov, J. Chang, M. Christl, A. R. Fazely, O. Ganel, R. M. Gunasingha, T. G. Guzik, J. Isbert, K. C. Kim, E. N. Kouznetsov, M. I. Panasyuk, W. K. H. Schmidt, E. S. Seo, N. V. Sokolskaya, J. W.

- Watts, J. P. Wefel, J. Wu, and V. I. Zatsepin, ArXiv Astrophysics e-prints (2006), astro-ph/0612377.
 [2] H. S. Ahn, P. Allison, M. G. Bagliesi, J. J. Beatty, G. Bigongiari, J. T. Childers, N. B. Conklin, S. Coutu, M. A. DuVernois, O. Ganel, J. H. Han, J. A. Jeon, K. C.

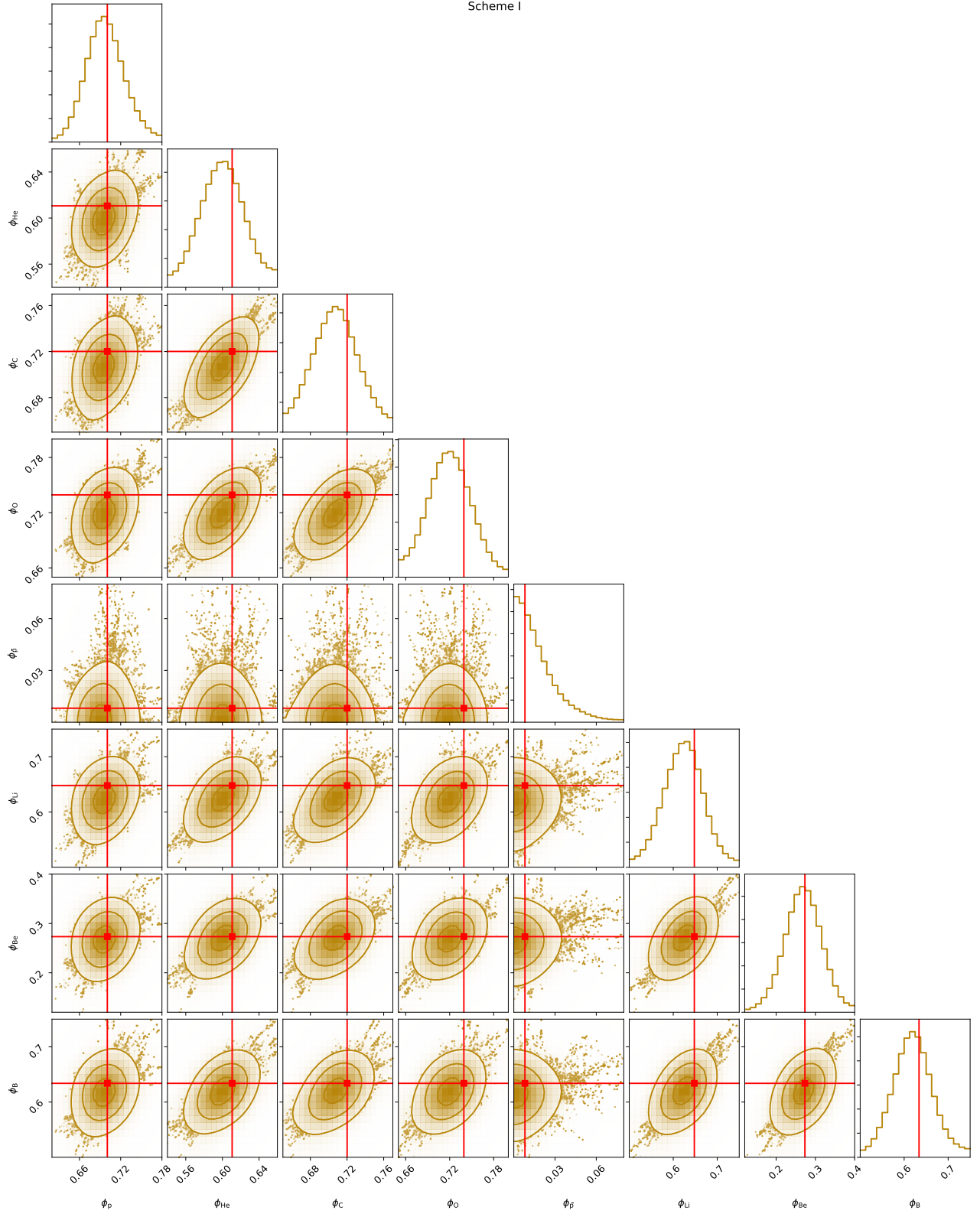


FIG. 10: Fitting 1D probability and 2D credible regions of posterior PDFs for the combinations of all solar modulation potentials from Scheme I. The regions enclosing σ , 2σ and 3σ CL are shown in step by step lighter golden. The red cross lines and marks in each plot indicates the best-fit value (largest likelihood).

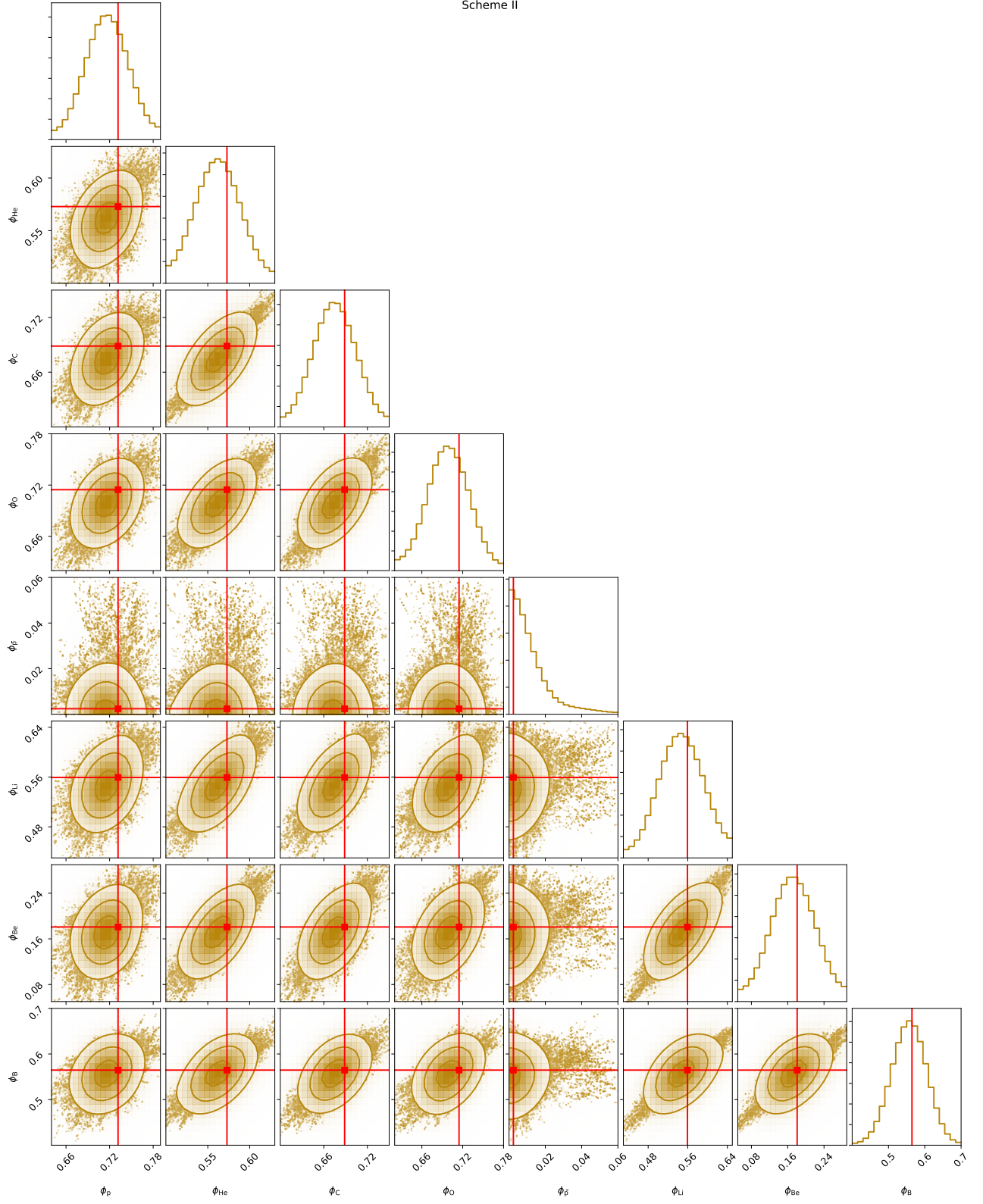


FIG. 11: Same as Fig. 10, but for Scheme II.

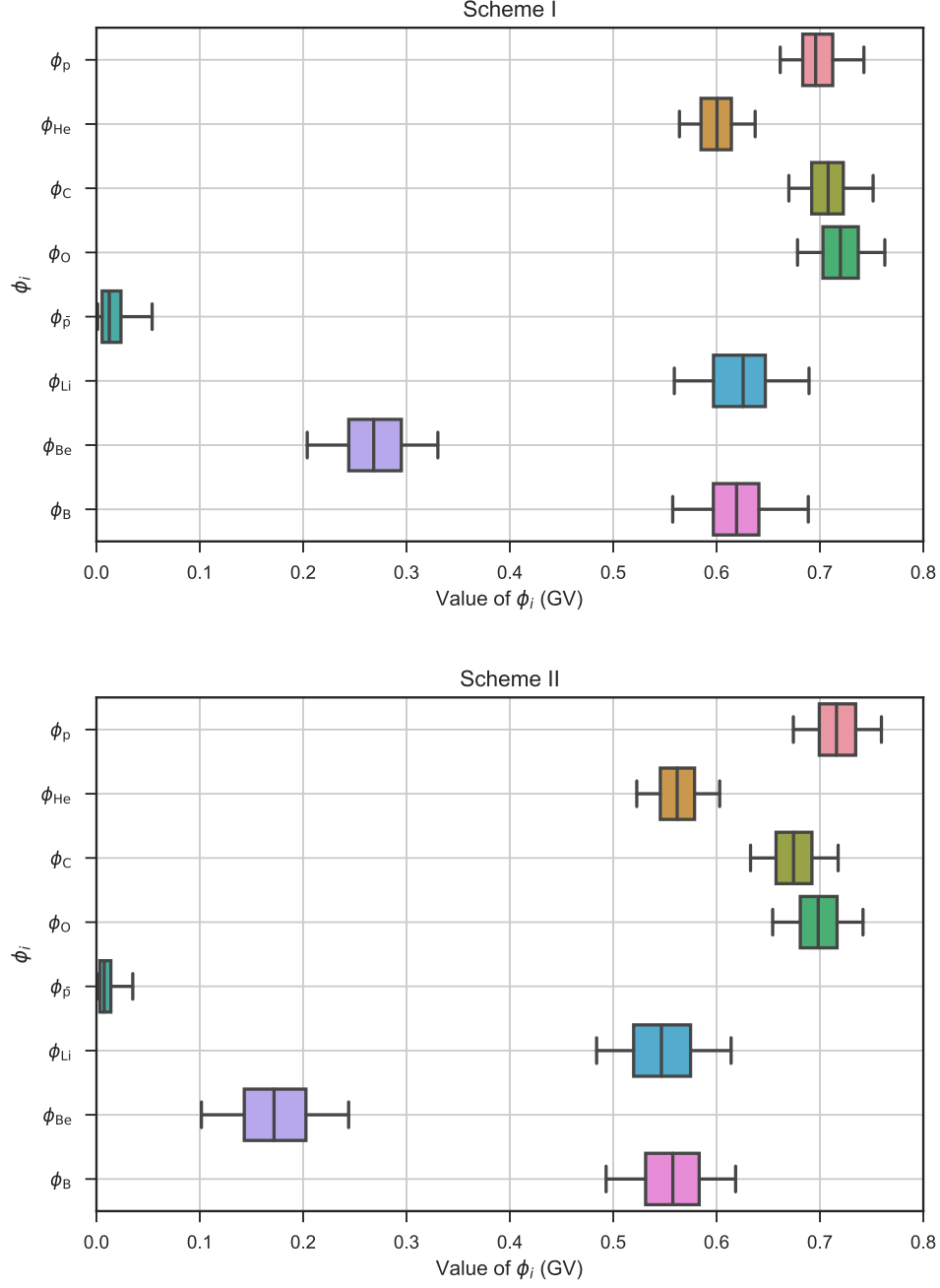


FIG. 12: The boxplot for the solar modulation potentials (ϕ_i s) in Scheme I and II.

- Kim, M. H. Lee, L. Lutz, P. Maestro, A. Malinin, P. S. Marrocchesi, S. Minnick, S. I. Mognet, J. Nam, S. Nam, S. L. Nutter, I. H. Park, N. H. Park, E. S. Seo, R. Sina, J. Wu, J. Yang, Y. S. Yoon, R. Zei, and S. Y. Zinn, *Astrophys. J. Lett.* **714**, L89 (2010), arXiv:1004.1123 [astro-ph.HE].
- [3] PAMELA Collaboration, O. Adriani, G. C. Barbarino, G. A. Bazilevskaya, R. Bellotti, M. Boezio, E. A. Bogomolov, L. Bonechi, M. Bongi, V. Bonvicini, S. Borisov, and et al., *Science* **332**, 69 (2011), arXiv:1103.4055 [astro-ph.HE].
- [4] AMS Collaboration, M. Aguilar, D. Aisa, B. Alpat, A. Alvino, G. Ambrosi, K. Andeen, L. Arruda, N. Attig, P. Azzarello, A. Bachlechner, and et al., *Physical Review Letters* **114**, 171103 (2015).
- [5] AMS Collaboration, M. Aguilar, D. Aisa, B. Alpat, A. Alvino, G. Ambrosi, K. Andeen, L. Arruda, N. Attig, P. Azzarello, A. Bachlechner, and et al., *Physical Review Letters* **115**, 211101 (2015).
- [6] M. Aguilar, L. Ali Cavazonza, B. Alpat, G. Ambrosi, L. Arruda, N. Attig, S. Aupetit, P. Azzarello, A. Bachlechner, F. Barao, and et al. (AMS Collaboration), *Phys.*

- Rev. Lett. **119**, 251101 (2017).
- [7] M. Aguilar, L. Ali Cavazonza, G. Ambrosi, L. Arruda, N. Attig, S. Aupetit, P. Azzarello, A. Bachlechner, F. Barao, and et al. (AMS Collaboration), Phys. Rev. Lett. **120**, 021101 (2018).
 - [8] M. Korsmeier and A. Cuoco, ArXiv e-prints (2016), arXiv:1607.06093 [astro-ph.HE].
 - [9] M. J. Boschini, S. Della Torre, M. Gervasi, D. Grandi, G. Jóhannesson, M. Kachelriess, G. La Vacca, N. Masi, I. V. Moskalenko, E. Orlando, S. S. Ostapchenko, S. Pensotti, T. A. Porter, L. Quadroni, P. G. Rancoita, D. Rozza, and M. Tacconi, Astrophys. J. **840**, 115 (2017), arXiv:1704.06337 [astro-ph.HE].
 - [10] J.-S. Niu, T. Li, R. Ding, B. Zhu, H.-F. Xue, and Y. Wang, Phys. Rev. D **97**, 083012 (2018), arXiv:1712.00372 [astro-ph.HE].
 - [11] J.-S. Niu, T. Li, and F.-Z. Xu, ArXiv e-prints (2017), arXiv:1712.09586 [hep-ph].
 - [12] C.-R. Zhu, Q. Yuan, and D.-M. Wei, Astrophys. J. **863**, 119 (2018), arXiv:1807.09470 [astro-ph.HE].
 - [13] Y. Génolini, P. D. Serpico, M. Boudaud, S. Caroff, V. Poulin, L. Derome, J. Lavalley, D. Maurin, V. Poireau, S. Rosier, P. Salati, and M. Vecchi, Physical Review Letters **119**, 241101 (2017).
 - [14] P. Blasi, E. Amato, and P. D. Serpico, Physical Review Letters **109**, 061101 (2012), arXiv:1207.3706 [astro-ph.HE].
 - [15] N. Tomassetti, Astrophys. J. Lett. **752**, L13 (2012), arXiv:1204.4492 [astro-ph.HE].
 - [16] N. Tomassetti, Astrophys. J. Lett. **815**, L1 (2015), arXiv:1511.04460 [astro-ph.HE].
 - [17] N. Tomassetti, Phys. Rev. D **92**, 081301 (2015), arXiv:1509.05775 [astro-ph.HE].
 - [18] J. Feng, N. Tomassetti, and A. Oliva, Phys. Rev. D **94**, 123007 (2016), arXiv:1610.06182 [astro-ph.HE].
 - [19] Y.-Q. Guo and Q. Yuan, Phys. Rev. D **97**, 063008 (2018), arXiv:1801.05904 [astro-ph.HE].
 - [20] A. E. Vladimirov, G. Jóhannesson, I. V. Moskalenko, and T. A. Porter, Astrophys. J. **752**, 68 (2012), arXiv:1108.1023 [astro-ph.HE].
 - [21] G. Bernard, T. Delahaye, Y.-Y. Keum, W. Liu, P. Salati, and R. Taillet, Astron. Astrophys. **555**, A48 (2013), arXiv:1207.4670 [astro-ph.HE].
 - [22] S. Thoudam and J. R. Hörandel, Mon. Not. Roy. Astron. Soc. **435**, 2532 (2013), arXiv:1304.1400 [astro-ph.HE].
 - [23] N. Tomassetti and F. Donato, Astrophys. J. Lett. **803**, L15 (2015), arXiv:1502.06150 [astro-ph.HE].
 - [24] J.-S. Niu and T. Li, Phys. Rev. D **97**, 023015 (2018), arXiv:1705.11089 [astro-ph.HE].
 - [25] Q. Yuan, S.-J. Lin, K. Fang, and X.-J. Bi, ArXiv e-prints (2017), arXiv:1701.06149 [astro-ph.HE].
 - [26] Q. Yuan, C.-R. Zhu, X.-J. Bi, and D.-M. Wei, ArXiv e-prints (2018), arXiv:1810.03141 [astro-ph.HE].
 - [27] L. J. Gleeson and W. I. Axford, Astrophys. J. **154**, 1011 (1968).
 - [28] A. W. Strong and I. V. Moskalenko, Astrophys. J. **509**, 212 (1998), astro-ph/9807150.
 - [29] I. V. Moskalenko, A. W. Strong, J. F. Ormes, and M. S. Potgieter, Astrophys. J. **565**, 280 (2002), astro-ph/0106567.
 - [30] A. W. Strong and I. V. Moskalenko, Advances in Space Research **27**, 717 (2001), astro-ph/0101068.
 - [31] I. V. Moskalenko, A. W. Strong, S. G. Mashnik, and J. F. Ormes, Astrophys. J. **586**, 1050 (2003), astro-ph/0210480.
 - [32] V. S. Ptuskin, I. V. Moskalenko, F. C. Jones, A. W. Strong, and V. N. Zirakashvili, Astrophys. J. **642**, 902 (2006), astro-ph/0510335.
 - [33] G. Jóhannesson, R. Ruiz de Austri, A. C. Vincent, I. V. Moskalenko, E. Orlando, T. A. Porter, A. W. Strong, R. Trotta, F. Feroz, P. Graff, and M. P. Hobson, Astrophys. J. **824**, 16 (2016), arXiv:1602.02243 [astro-ph.HE].
 - [34] AMS Collaboration, M. Aguilar, L. Ali Cavazonza, B. Alpat, G. Ambrosi, L. Arruda, N. Attig, S. Aupetit, P. Azzarello, A. Bachlechner, F. Barao, and et al., Physical Review Letters **117**, 091103 (2016).
 - [35] R. Aloisio, P. Blasi, and P. D. Serpico, Astron. Astrophys. **583**, A95 (2015), arXiv:1507.00594 [astro-ph.HE].
 - [36] M. J. Boschini, S. Della Torre, M. Gervasi, G. La Vacca, and P. G. Rancoita, ArXiv e-prints (2017), arXiv:1704.03733 [astro-ph.SR].
 - [37] M. E. Wiedenbeck, N. E. Yanasak, A. C. Cummings, A. J. Davis, J. S. George, R. A. Leske, R. A. Mewaldt, E. C. Stone, P. L. Hink, M. H. Israel, M. Lijowski, E. R. Christian, and T. T. von Rosenvinge, Space Sci. Rev. **99**, 15 (2001).
 - [38] M. E. Wiedenbeck, W. R. Binns, A. C. Cummings, G. A. de Nolfo, M. H. Israel, R. A. Leske, R. A. Mewaldt, R. C. Ogliore, E. C. Stone, and T. T. von Rosenvinge, International Cosmic Ray Conference **2**, 149 (2008).
 - [39] Y. Génolini, D. Maurin, I. V. Moskalenko, and M. Unger, Phys. Rev. C **98**, 034611 (2018), arXiv:1803.04686 [astro-ph.HE].
 - [40] D. Maurin, F. Melot, and R. Taillet, Astron. Astrophys. **569**, A32 (2014), arXiv:1302.5525 [astro-ph.HE].
 - [41] D. Foreman-Mackey, W. Voudsen, A. Price-Whelan, M. Pitkin, V. Zabalza, G. Ryan, Emily, M. Smith, G. Ashton, K. Cruz, W. Kerzendorf, T. A. Caswell, S. Hoyer, K. Barbary, I. Czekala, D. W. Hogg, and B. J. Brewer, “corner.py: corner.py v1.0.2,” (2016).